AGU100 ADVANCING EARTH AND SPACE SCIENCE

Water Resources Research

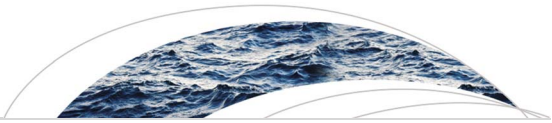

RESEARCH ARTICLE
10.1029/2017WR021954

Key Points:
- Experiments with layers, vertical and horizontal, of nearly monodisperse particles to create size contrast with controlled IR heating from above to mimic solar radiative heating
- Deposited fluorescein particles show final sites of drying; color contrast between an evaporating and a draining zone is made clear
- Surface temperature fields with IR imaging distinguish wet and dry regions on the surface and gives relation to evaporation rates

Supporting Information:
- Supporting Information S1

Correspondence to:
N. Kumar,
navneet01011987@gmail.com

Citation:
Kumar, N., & Arakeri, J. H. (2018). Evaporation from layered porous medium in the presence of infrared heating. *Water Resources Research*, *54*, 7670–7687. https://doi.org/10.1029/2017WR021954

Received 26 SEP 2017
Accepted 18 SEP 2018
Accepted article online 24 SEP 2018
Published online 12 OCT 2018

Evaporation From Layered Porous Medium in the Presence of Infrared Heating

Navneet Kumar[1] and **Jaywant H. Arakeri**[1]

[1]Department of Mechanical Engineering, Indian Institute of Science, Bangalore, India

Abstract We report an experimental study of evaporation of two configurations of layered porous media that are heated from above by infrared (IR) radiation having ~1,000 W/m^2 intensity. We used nearly monodisperse glass beads in each of the layers. The two configurations are (1) coarse and fine beads, stacked side by side and (2) fine beads over coarse beads (FoC). The IR heater mimics the natural evaporation process in soils, and the aim is to study, using three diagnostic tools, how the layering affects the evaporation process, and compare it with the homogeneous porous medium case. For each experiment we use three diagnostics simultaneously, evaporation rate measurement using a precision balance, surface temperature imaging using an IR camera, and visualization of the evaporation process with fluorescein dye. The constant (evaporation) rate period (CRP) regime, found in homogeneous porous media, is drastically changed for the two layered configurations. We show new results for side-by-side configuration. In the FoC configuration we show that the near-surface water content in the finer particles does not change in CRP and a true constant evaporation rate is possible. The average water depth at end of CRP in the porous medium, for a wide range of diameter ratios for the FoC configuration are compared with the predictions from theoretical relations proposed by Shokri et al. (2010, https://doi.org/10.1029/2009JB006743) and Assouline et al. (2014, https://doi.org/10.1002/2013WR014489). Using a simple surface energy budget, we show that knowing the surface temperature, the evaporation rate can be estimated with reasonable accuracy (±5%) during drying of a porous medium.

Plain Language Summary We show the movement of water from larger particle sizes to the smaller in different combinations of texturally layered systems. Temperature, measured using an infrared camera, was used as a tracer to track surface water content. In the subsurface we tracked the drying front using a *unique* fluorescein dye visualization technique. The dye particles are red when dry but appear green in solution with water.

1. Introduction

Evaporation characteristics of a homogeneous porous medium have been studied extensively and its three stages (first stage or constant rate period or CRP, transition regime or falling rate period or FRP, and second stage or receding front period or RFP) are an established fact (Lehmann et al., 2008; Or et al., 2013; Sherwood, 1929, and references therein; Kumar & Arakeri, 2018a). Simple 2-D models (Schlünder, 1988; Suzuki & Maeda, 1968) have captured the essential features of evaporation from a periodic array of small water sources separated by dry regions. These models are for the situation where water is present just below the porous medium top surface, and they show that even for small open area fractions (such as 10%), evaporation rate was comparable to that of a bare water source. The formation of multidimensional vapor shells (Bange, 1953; Brown & Escombe, 1900; Cooke, 1967; Stefan, 1881) over individual evaporating sources and their interaction with the ambient (Shahraeeni et al., 2012) has been attributed for the observed high evaporation rate during CRP. It has been further shown that high evaporation rates can also be maintained due to films (Yiotis et al., 2004), which transport water from within the porous medium to its top surface. Neutron-based imaging techniques (Ketelaars et al., 1995; Pel et al., 1993; Shokri et al., 2008; Valckenborg et al., 2001), such as neutron magnetic resonance, have been successfully used in capturing the water content within during drying of a porous medium. Near-surface distribution of water in a porous medium for a considerably higher duration (and saturation values) suggested the presence of these films (Thiery et al., 2017) even in nanometric dimensions. The presence of water, in CRP regime, near the porous medium top surface was clearly captured by IR imaging (Kumar & Arakeri, 2018a). The CRP regime has also been found in other geometries, polygonal capillaries (square in Chauvet et al., 2009, 2010, and rectangular in Keita et al., 2016) and vertically stacked circular rods (Kumar & Arakeri, 2018b) and has been shown to be due to corner films.

The duration of CRP regime is usefully given in terms of the average depth of water at the end of CRP (L_{cap}) and has been termed as capillary characteristic length (Lehmann et al., 2008; Shokri et al., 2010; Yiotis et al., 2012). We may consider two classes of evaporation and transition from CRP. One is a capillary-gravity regime where the porous medium height (H) is greater than L_{cap} and there is true transition from CRP; at the end of CRP a saturated layer will be present at the bottom of the porous medium and L_{cap} will be independent of H. The other is capillary regime (Assouline et al., 2014) where the evaporation is from porous media with short heights less than L_{cap}. In this case, transition will happen when the whole porous medium is depleted of water. The fact that duration of CRP is affected by H has been shown in a few earlier studies (Assouline et al., 2014; Gardner & Hanks, 1966; Lehmann et al., 2008). Kumar (2016) reports several cases of transition to CRP in shallow containers. For a homogeneous medium with nearly monodisperse spherical beads, Kumar and Arakeri (2018a) found a drastic decrease in L_{cap} with increasing particle size. Note that in case of monodisperse particles the pore size distribution, backbone of the model presented in Lehmann et al. (2008) can be neglected. One main question in the present study is how will the L_{cap} value changes in a layered porous medium?

Textural layering has been studied by soil scientists for more than half a century. Two simplest types of horizontal textural layering are (1) finer over coarser (FoC) and (2) coarser over finer (CoF). Of course, in real situations the layering is more complex. Previous investigators have shown that the textural layering not only affects the evaporation process but can also change water movement beneath (Ross, 1990) significantly. The major influencing factors are layer thicknesses, their sequence and slope, and the individual layer characteristics. FoC situation is generally termed as the *capillary barrier* in the literature. In this scenario, the percolating liquid is retained in the finer particles and also at the interface of the finer and coarser particles and penetration into the coarser particles is inhibited. The findings of Bruch (1993) have been used extensively in creating capillary barriers. He showed that the FoC case resulted in sustained evaporation rates for longer time, while in CoF case the hydraulic connections were broken earlier. The other configuration, viz., CoF is sometimes called *hydraulic barrier*, helps in limiting the permeability and has been used successfully to suppress evaporation. Mathematically, Poulovassilis and Psychoyou (1985) reported separate conditions for sustained maximum and minimum hydraulic conductivities in case of FoC and CoF configurations, respectively. A recent review by Li et al. (2013) focuses on some of these issues. The CoF configuration, also known as *mulching*, is used extensively in the agricultural sector. Numerous experimental (Assouline et al., 2014; Huang, Philip, & Barbour, 2013; Modaihsh et al., 1985; Shokri et al., 2010; Unger, 1971; Willis, 1960; Yuan et al., 2009; Zhao et al., 2017) and numerical models (Pillai et al., 2009; Wang, 2015) have shown reduced evaporation rates, at some time, for a CoF configuration compared to a homogeneous porous medium having the particle size same as the finer one; the transition to low rates of evaporation were observed to occur earlier for CoF case compared to the homogeneous one. Vertical layering where two (or more) differently sized particles are placed side by side has received less attention. Lehmann and Or (2009) studied such a configuration in a Hele-Shaw cell where experiments were conducted in the absence of any external heat source. Capillary-induced transport of water from the coarser to the finer regions was clearly shown; porous column was high enough for a capillary-gravity regime to exist and to capture true transition from stage 1 to stage 2. They did not study the surface temperature distribution. In a recent article, Aminzadeh and Or (2014) performed experiments on evaporation from a different type of heterogeneity—inclusions consisting of fine particles in a coarser medium. Surface temperature distribution was obtained using IR imaging and an analysis was done of the energy partitioning.

More interesting is the FoC configuration. Willis (1960) experimentally found very little difference between the evaporation rates of the homogeneous finer soils and the FoC soil configuration, though the hydraulic conductivity has been found to be higher in the latter case (Eagleman & Jamison, 1962; Srinilta et al., 1969; Warrick & Yeh, 1990). However, decreased hydraulic conductivity was reported (Warrick & Yeh, 1990) for the four-layer (FoCoFoC) case compared to the two-layer case (FoC) and was argued to be due to the second layer (coarser) acting as mulch for the third layer (finer). Huang, Philip, and Barbour (2013) measured the soil water content profile with height and showed that water content was much higher in the finer size compared to coarser size. In all the cases, the soil water content varied sharply at the interfaces. Huang, Barbour, et al. (2013) argued that the capillary barrier (FoC configuration) can significantly enhance the plant available water that can further increase the leaf area index and potential productivity. Capillary barrier, however, may be detrimental to plants since it can inhibit oxygen transport. Higher L_{cap} values are reported experimentally

in Shokri et al. (2010) for the cases with higher layer thickness of the finer particles on top. In the FoC configuration Assouline et al. (2014) varied the finer size layer thickness while keeping the total columnar height of the porous medium constant. In all the experiments in this configuration the height of the finer size was less than its corresponding L_{cap}. They found that L_{cap} increases with increasing layer thickness of the finer size. In both the experimental studies, the particles in each layer had a range of sizes; they were not monodisperse.

Most of the previous studies were conducted with natural soil or polydisperse sizes where the particles had a range of sizes. The range of sizes has a substantial effect on L_{cap} even for a homogeneous porous medium as reported in Lehmann et al. (2008). Additionally, in layered (treated by others as a type of heterogeneity) media, there is the complexity of intermixing between the particles; if finer particles are small enough they may enter the voids between the coarser particles driven either by gravity or capillarity. In these situations, therefore, it is difficult to assess the effects of individual particle sizes and interaction between them on the overall evaporation characteristics. We resolve this issue by using *nearly monodisperse spheres* (spheres size in a narrow range) in each layer and present results on the textural layering in two configurations—(a) evaporation from layers of two differently sized glass beads stacked side by side and (b) evaporation from layers of glass beads in FoC configuration. The experiments conducted here are with two layers of nearly monodisperse particles, having a narrow range of bead sizes, under controlled IR heating. Repeatability of experimental observations was ensured by conducting multiple runs for each case. The side-by-side configuration has been relatively less studied (one such study is Lehmann & Or, 2009), and here we show that this simple configuration yields clear results on the water movement driven by pore size difference and its effect on evaporation rate and temperature distribution on the top surface. For the vertical layering, we concentrate mainly on the FoC configuration and results with the CoF configuration are discussed in brief. In natural systems the layering is more complex. The side-by-side and horizontally layered configurations may be considered as simple model systems, for understanding and modeling the transport of water in locally heterogeneous regions found in soils. The aim of the present study is twofold: one in these simple layered systems to study in detail the processes of evaporation and water movement under controlled IR heating, which mimics solar heating, and two, to give information of evaporation rates, surface temperature data and L_{cap} values. We believe this information will be of value in developing models to predict evaporation and water movement in the more complex porous media obtained in natural systems.

2. Materials and Methods

Experiments were conducted with nearly monodisperse glass beads (GB) with 95% sphericity. The diameter ranges of the GB used varied from 0.10–0.16 to 2.5–3.0 mm. The mixture of spherical beads saturated with deionized water was placed in acrylic or glass containers. The experimentally obtained porosities (~35%) resulted from a fixed procedure of the sample preparation, which was done carefully to maximize the packing fraction. Detailed sample preparation protocol is given in Kumar (2016), and here we briefly give the main steps. The container is filled with a small amount (~2-mm layer height) of the water, with fluorescein dye added if required. The glass beads were dropped slowly into the container, which is continuously and slowly shaken manually until there is no extra water on the top. More water is then added, and same procedure is followed till we reach the desired height of the porous column. Note that in the side-by-side case, a thin (1 mm in thickness) glass plate was placed vertically at the center of the box which separates the container in two nearly equal compartments. These halves were filled separately (following the protocol) with the two different bead sizes such that their heights are nearly equal. The glass plate was eventually removed slowly while the container was shaken carefully, which allowed the beads to settle.

The container was insulated from all the sides except at the top from where evaporation occurs. The sample was heated radiatively from the top using a 20 × 20 cm flat ceramic IR heater whose intensity was controlled using a variac; as mentioned this as an important new feature of the present work as most of the previous studies were conducted in absence of any heating and is used to mimic the surface heating due to solar radiation. IR radiation is used, instead of the full solar spectrum, so that almost all the radiation is absorbed in the top few microns of the glass beads or water and thus is close to surface heating. To reduce unnecessary heat gain, reflector sheets (shiny aluminum foil) were added to the outside surfaces of the insulation as well as to the top inner surface of the container. Heat flux received by the top surface of the sample was nearly 1,000 W/m^2 corresponding to a distance of 18.5 cm between the IR heater and the sample. Mass loss was

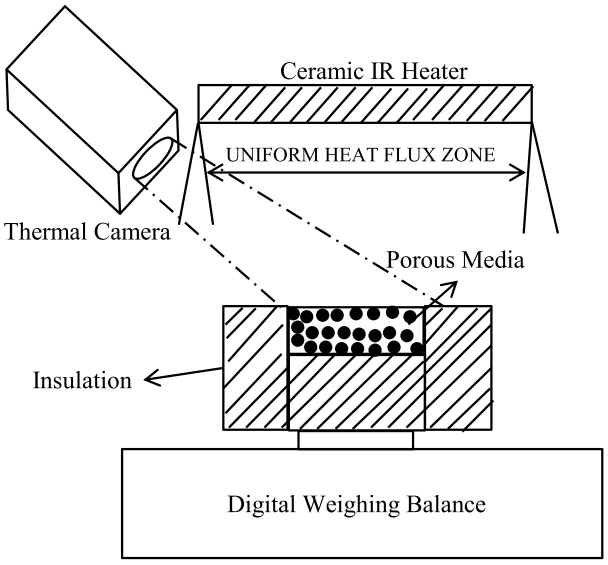

Figure 1. Schematic of the experiment setup. A digital precision weighing balance is used to monitor mass loss, ceramic infrared heater heats the evaporating surface from above. A thermal camera, fixed at an angle measures the surface temperature of the top surface of the porous medium.

monitored using a precision weighing balance (Sartorius GPA5202 with a least count of 0.01 g); mass was recorded on a computer every 15 s. A thermal camera (Fluke Ti400, 320 × 240 pixels) was used to monitor the porous medium top surface temperature; the temperatures were recorded at an interval of ~30 min in most of the experiments. The thermal camera kept at a fixed vertical inclination (~25°) with respect to the drying surface since IR heater was kept exactly above. As we shall see below, the surface temperature helps in detecting the wet and dry regions near the surface. A T-type thermocouple was used to measure the ambient temperature. A T-type thermocouple was used to measure the ambient temperature. A Honeywell humidity sensor (HIH-4000 with an accuracy of 2%) was used to measure the relative humidity in the ambient away from the heating zone. A schematic of the experimental setup is shown in Figure 1. The emissivity in the thermal camera was set to 0.92 & 0.95 for GB and deionized water respectively. Reflected radiation increased the surface temperature sensed by the camera by nearly 5–6 °C for the glass beads at an incident heat flux of 1,000 W/m^2. IR radiation was thus blocked for a few seconds in order to measure the true top surface temperature. The few seconds of blockage of IR radiation produced negligible reduction in the surface temperature. Evaporation sites in a porous medium were tracked using the fluorescein dye technique (Kumar & Arakeri, 2018a); a similar technique was used by previous investigators (Shokri et al., 2010, and references therein; Keita et al., 2013). Originally orange colored fluorescein dye particles turns green when mixed with water. This feature essentially helped us in determining whether a region, at a small length scale (bead size) or larger length scale, is wet or dry. A dry surface over which evaporation would have occurred earlier leaves orange deposits of dye particles and a region which is still wet would appear green.

3. Surface Energy Budget for Nonisothermal Drying

In drying of a porous medium the evaporative flux is coupled with its surface temperature, which is evident using a simple surface energy budget (SEB). In the so-called isothermal case, evaporating porous medium gains energy from the ambient; phase change (latent heat loss) leads to cooling and subatmospheric surface temperature. With external surface heating, as from solar radiation, temperature of the surface usually is more than the ambient which results in convective and radiative heat loss to the ambient. SEB essentially is a relation between the incoming heat and different types of heat losses (Aminzadeh & Or, 2013, 2014; Mauder et al., 2007; Qiu et al., 1999, 2006). Consider the surface of a porous medium which is heated from above with radiative flux I_{total}. SEB gives

$$I_{\text{total}} = I_{\text{ref}} + I_{\text{rad}} + I_{\text{conv}} + I_{\text{cond}} + I_{\text{lat}} \tag{1}$$

where I_{ref}, I_{rad}, and I_{conv} are the reflected, net radiated, and convective heats lost from the surface into the ambient respectively. I_{cond} is the heat conducted from the surface to within the porous medium, sometimes, also referred as the ground heat flux. I_{lat} is the latent heat loss due to evaporation from the porous medium. Note that all the terms in equation (1) represent heat per unit area or heat flux (W/m^2). In terms of relevant parameters equation (1) can be written as

$$\epsilon_s I_{\text{total}} + \sigma\epsilon_a\epsilon_s(1 - f_{sh})T_a^4 = \sigma\epsilon_s T_s^4 - + h(T_s - T_a) + k_{eff}\nabla T + \frac{m_w^{'}\lambda}{A_s} \tag{2}$$

where, $A_s(m^2)$, ϵ_s, ϵ_a, and K_{eff} (W/mK) are respectively the surface area, the emissivities of the porous medium top surface and the ambient, and the effective thermal conductivity of the surface. T_s and T_a are the temperatures of the porous medium top surface and in the ambient respectively (K). $m_w^{'}$ is the mass loss rate (kg/s), λ is the latent heat of vaporization (kJ/kg), and σ is the Stefan-Boltzmann constant. The operator (∇) represents the spatial gradient. f_{sh} is the view factor from the top surface to the heater. The first term on the left-hand side of equation (2) is the net (incoming − reflected) IR radiation incident on the surface, and the second

term is the heat received by the surface from the ambient due to long-wave radiation. The terms on the right-hand side of equation (2) are the different heat losses from the surface. We calculated f_{sh} to be ~0.27 for the dimensions corresponding to our experimental setup. h is the convective heat transfer coefficient which is obtained using Nusselt (Nu)-Rayleigh (Ra) correlations, with a finite characteristic length (l^*), for a flat surface in windless conditions (Lloyd & Moran, 1974). For the container dimensions and heating rates of the present study the following relation is used:

$$Nu = \left(\frac{hl^*}{k_a}\right) = 0.59Ra^{0.25}; 200 < Ra < 10^4 \tag{3}$$

where Ra is calculated based on the total density change of the vapor phase (for a wet surface change in density is due to both temperature difference and concentration difference of the evaporated vapors) and k_a is the thermal conductivity of air. Similar correlations exist for other ranges of Ra. Finally, the last remaining term is to model I_{cond} for which estimates of k_{eff} and ∇T are needed. Using networking approach, Zehner and Schlunder (1970) predicted relations for k_{eff} as a function of the thermal conductivities of solid and fluid components of the porous medium for fully saturated and fully unsaturated cases. For a semisaturated porous medium, however, the complexity of the existence of phases and their random distribution makes the prediction of k_{eff} nearly impossible.

For our experiments I_{cond} splits into two parts namely heat storage ($I_{heat\ stored}$) and heat loss through the insulation (I_{insul}) and into the ambient. After the initial transient period, heat storage is negligible in stage 1 and stage 2 but not during the transition. In these stages the heat loss through the insulation can be written as:

$$I_{cond} = I_{heat\ stored} + I_{insul} \sim I_{insul} = k_{loss}(T_s - T_a) \tag{4}$$

where, k_{loss} is the coefficient for heat loss through the insulation. We obtain k_{loss} using the evaporation rate value in the stage 2, essentially when the evaporation rates are very low. Using equations (2) and (4), a relation between $m_w^{'}$ and T_s is obtained:

$$\frac{m_w^{'}}{A_s} = \frac{E_w}{86.4} = \left(\frac{1}{\lambda}\right)\left[\epsilon_s I_{total} - \left\{\sigma\epsilon_s T_s^4 - \sigma\epsilon_a\epsilon_s(1 - f_{sh})T_a^4 + h(T_s - T_a) + k_{loss}(T_s - T_a)\right\}\right] \tag{5}$$

where E_w is the evaporation rate (mm/day). The obtained k_{loss} value is used to estimate E_w at all the other instants. Equation (5) suggests that for a fixed I_{total} an increase in T_s leads to a decrease in E_w and vice versa. This equation is useful to predict the evaporation rates of a drying porous medium based only on the surface temperature and the atmospheric conditions including the incoming heat intensity. We note that at the field level, extensive work has been done to estimate evaporative flux using SEB and models of different complexity have been proposed (see, e.g., Daamen & Simmonds, 1996; Kalma et al., 2008). Many of these studies are at large scales, using satellite imagery to get surface temperatures. Our interest, however, in the present work, is to use SEB for the laboratory experiment where the conditions are less complex. Note that equation (5) is an indirect way of estimating the rate of evaporation and differs from the standard vapor pressure deficit (VPD) formulation. When the surface is wet, evaporation takes place from the top surface, and the VPD can be directly calculated. If the surface is dry, then evaporation takes place from the vaporization plane within the porous medium. Of course, if the surface vapor concentration is known, we can still use the VPD formulation to calculate the evaporation rate. The vapor concentration at the exposed surface, which will be lower, may be calculated accounting for the concentration drop or resistance from the vaporization plane to the top surface. But an additional calculation for the drop in concentration within the porous medium is required accounting for the conduction of heat from the top to the vaporization plane and flow resistance for the vapor through the pores. The SEB offers an alternate way to calculate the drying rates if the individual terms can be estimated or modeled. In the transient phase, the heat storage term may not be negligible. One uses the energy budget, including the latent heat term, whereas VPD directly looks at the gradient of concentration of water vapor at the surface, which, however, is coupled to the temperature and velocity fields. For general use of SEB, the heat conducted into the soil will need to be inputted. In our experiments, since the porous medium is confined and insulated, this term through K_{loss} is easily estimated.

4. Results

In this section we discuss results for the different configurations. First in section 4.1, we present evaporation characteristics of a mixture of two differently sized glass beads stacked side by side using standard evaporation curves, visualization using fluorescein dye technique, and thermal imaging. Movement of water and the drying front within the porous medium during evaporation in the FoC configuration is discussed next in section 4.2 in case of a shallow porous column. Finally, in case of large porous columns in section 4.3, we discuss how FoC configuration changes the evaporative length scales when compared to a homogeneous porous medium and also compare them to the theoretically determined length scales.

4.1. Capillary Regime: Mixture of Glass Beads Stacked Side by Side

For this configuration we put the finer (0.10- to 0.16-mm diameter) and coarser (0.70- to 0.85-mm diameter) glass beads on the left and right sides respectively in an acrylic box. The aim here is to understand the preferential water movement leading to partial drying of the top surface and characterize it. The depths of both the glass beads size are approximately same and their top surfaces were horizontal. The height of the acrylic box and the depth of the porous medium were 40 and 21.5 mm, respectively. The overall porosity of the porous medium was approximately 37.5%. The depth of the porous medium was less than the capillary film lengths (Kumar, 2016) for both the coarser and finer beads and thus the evaporation occurs in the capillary regime (Assouline et al., 2014). A similar stacking was used by Shahraeeni and Or (2011) where the focus was on the evolution of subsurface temperature rather than the surface temperature.

4.1.1. Visualization Using Fluorescein Dye and Characteristic Evaporation Curves

A series of snapshots of the porous medium were taken at different times as evaporation proceeded which are shown in Figure 2 along with their viewing direction. A small amount (0.6% by weight) of fluorescein dye was put in the water at the beginning of the experiment. Fluorescein dye in solution appears green; evaporation of the water on a surface leaves fluorescein particles, which are orange in color. For imaging the box was taken out of the insulation, shot at different angles and was put back. The imaging took 2.5–3 min, which was not found to affect the evaporation dynamics. Different views are marked corresponding to each column as seen in Figure 2. Also shown are the corresponding saturation values at these instants.

Figures 2a–2d taken just before the beginning of the experiment show the green color solution. At t = 2.16 hr (S = 0.78), evaporation on the coarser beads side shows deposits of fluorescein dye particles, slightly orange color, in the top view (Figure 2e), and dry patches near the top in the side views (Figures 2f and 2g). In contrast, the finer glass beads side (Figures 2e and 2h) is still green, indicating saturation. The finer glass beads because of the lower void size suck out all the water present in the coarser glass beads except for that present in the form of pendular structures. This can also be thought in terms of water potential as the driving force; in the present case water potential is due to the different surface tension forces in the two sizes. Till t = 5.16 hr (Figures 2i–2l) preferential evaporation takes place from the finer glass beads, while water from the coarser beads moves to the finer beads, but there is still some evaporation from the coarser beads side. Deposited fluorescein particles seen as orange color in Figures 2i and 2k near the top show the final evaporation sites from the top surface of the coarser glass beads. Figure 2j shows an interesting situation, where the finer glass beads are completely wet, while the coarser glass beads are nearly completely dry. At this instant, transition to second stage of evaporation (forced transition) has happened in the coarser glass beads and thus its contribution to the total evaporation rate becomes negligible. Small traces of water seen in Figure 2j are trapped in between the glass beads and the container wall (they will also be present in between the glass beads away from the wall) in the form of pendular structures. After this time, with the source from the coarser side depleted, water content in the finer beads, till now saturated, reduces due to evaporation. At t = 5.75 hr, we see the boundaries of the acrylic box, sites of maximum local porosity, are drained first (Figures 2n and 2p). Deposited fluorescein particles are seen in Figures 2m and 2q over the top surface of the finer glass beads. With time the boundaries in the finer glass beads start getting drained (Figures 2r and 2t) after which drainage continues within the inner zones of the finer glass beads until transition. Figures 2u–2x show the fully deposited fluorescein particles on the top surface of the porous medium and also at the interface of the finer and coarser glass beads. The side views (Figures 2v–2x) show a thinner layer of dye deposits on the finer beads side compared to the coarser side. Deposition of dye, initially mixed with water, due to evaporation have been studied in homogeneous porous media (Keita et al., 2013; Kumar & Arakeri, 2018a; Lehmann et al., 2008) and in layered porous media (Shokri et al., 2010). The transfer (lateral movement) of

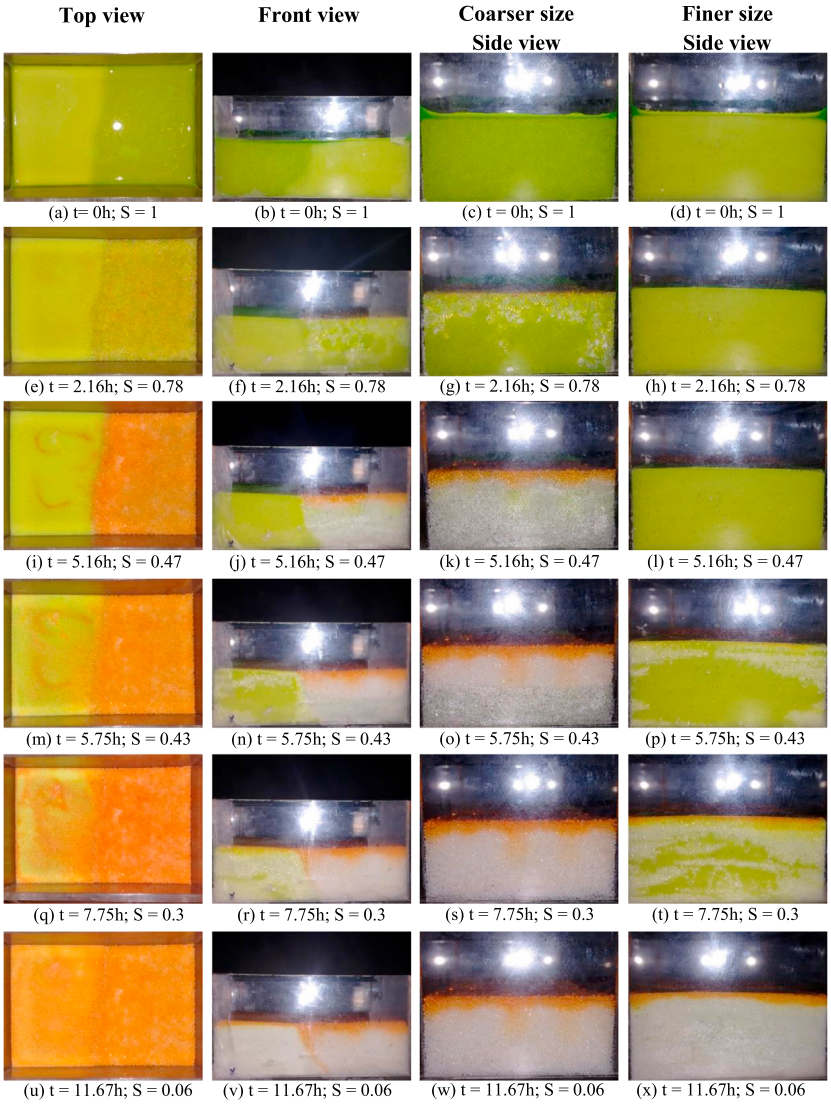

Figure 2. A series of snapshots showing the condition of the porous medium at different instants of the experiment. Columns 1 and 2 show the top and front views of the porous medium respectively, column 3 show the side view where the coarser size glass beads were packed, and column 4 shows the side view where the finer size glass beads were packed. The times and the corresponding saturation values (S) are also shown. Heat flux received by the top surface = 1,200 W/m^2.

water from hydrophobic beads to hydrophilic beads in a side-by-side packed porous medium was clearly seen in the dye images of Shokri and Or (2013). Further using neutron images they showed that hydrophilic side remained wet for a higher degree of saturation while in the hydrophobic side water front kept on receding within the porous medium. Note that in their study, water motion, from one side to the other, was driven by the wettability contrast, while in the present case it is driven by the difference in the beads sizes.

We now discuss the evaporation characteristics corresponding to the visualizations shown in Figure 2, that is, for the side-by-side stacked case. Figure 3 shows different nondimensional evaporation rate curves versus time. The inset shows the raw experimental data of evaporated mass (m_w, along primary vertical axis) and the derived evaporation rate (e_w, along secondary vertical axis) plotted against time; these correspond to the same experiment for which the images are shown in Figure 2. First, we will discuss the raw data. Dips in the evaporation rates at different instants correspond to the times when the container was taken out for optical imaging which led to temporary cooling. The experiment repeated without removing the box showed that the evaporation rate characteristics were essentially same, except the evaporation rate versus

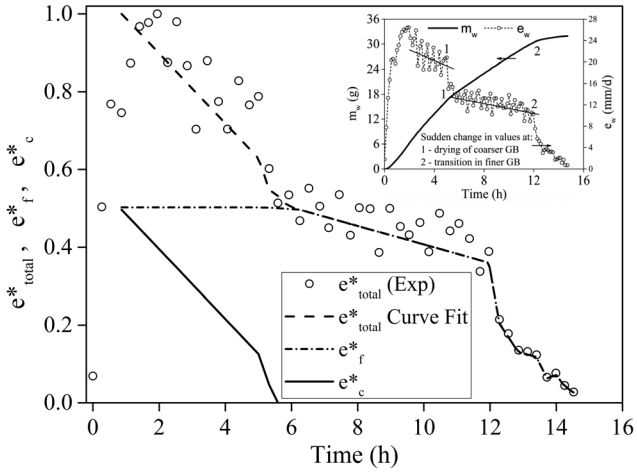

Figure 3. Variation of evaporated mass and evaporation rate versus time from a mixture of water and 0.10- to 0.16- and 0.70- to 0.85-mm diameter glass beads stacked vertically in an acrylic box. Sudden changes in the slope of the curve are marked at approximately $t = 5$ hr and $t = 12$ hr corresponding to the transition regime in the coarser and the finer glass beads respectively. Heat flux received by the top surface = 1,200 W/m^2.

time plot is smooth. With reference to the inset in Figure 3, water loss at the time of the first transition is about 18 g out of the total water mass of 36 g. The evaporation rate suddenly drops at around $t = 5$ hr (marked as *1*) and again at $t = 12$ hr (marked as *2*) corresponding to two transitions. The first drop in the evaporation rate at $t = 5$ hr, corresponds to the drying up of the coarser glass beads and its top surface becoming devoid of water. The value close to 14 mm/day at this instant (after first transition) is approximately half compared to 27 mm/day initially, in direct correlation with the reduction in surface area available for evaporation. Between $t = 5$ and $t = 12$ hr, the rate slowly goes down and the sudden drop at $t = 12$ hr corresponds to transition to the second stage in the finer beads side.

To better understand the evaporation processes, we plot (Figure 3) the evaporation rates normalized by the maximum value of the *fitted* evaporation rate curve; its value was ~28 mm/day at $t = 0.87$ hr. The normalized fitted evaporation rate curve, obtained by fitting to the data after the initial transients have died, is shown as a dashed line in Figure 3. The contribution from the individual bead sizes (e^*_c for coarser and e^*_f for finer) are estimated assuming a constant evaporation rate for the finer beads till $t = 5$ hr; this is a valid assumption since its top surface remains fully wet till this instant. We see that initially both e^*_c and e^*_f contribute equally but with time e^*_c decreases rapidly till $t = 5$ hr. This relatively large decrease in e^*_c is due to the coarser beads side losing water due to both evaporation (Stefan tube-like situation (Shahraeeni et al., 2012) where the menisci keeps receding from the top evaporating end) and to the finer beads side, as discussed in dye visualization section. Note that in the present case, the height of the porous medium is such that evaporation occurs in the capillary regime; larger porous column heights would be required for a capillary-gravity regime as in Lehmann and Or (2009).

4.1.2. Thermal Images

The migration of water from coarser to finer regions and the differences in the evaporation rates from the two regions is reflected in the surface temperature distribution. Figure 4 shows a series of thermal images of the top surface of the porous medium taken at different instants. Figure 4a is a schematic showing different regions captured in an IR image. The image size is 320 pixels by 240 pixels and each pixel represents the local surface temperature. The porous medium top surface is seen enclosed by a dashed line while the hatched regions represent the container walls. Rest of the regions in Figure 4a represent the insulation. Our interest lies in the temperature distribution within the dashed line. Note that the heat flux from the IR heater was about 1,200 W/m^2. In all the IR images, purple color represents lower temperatures and red represents higher temperatures. Note that a particular color cannot be assigned to a given temperature range since the surface temperature evolution is dynamic. The corresponding maximum (T_{max}) and minimum (T_{min}) surface temperatures, found on the exposed porous medium, are also given. Brown and gray colors have been assigned for temperatures lesser than T_{min} and greater than T_{max}, respectively; these colors also represent different temperature levels in the different images. Figure 4b shows the thermal image taken before the start of the experiment with temperature being close to the wet bulb temperature (~25 °C). Surface temperature increases soon after IR heater is switched on. In general, temperatures near the boundary walls are higher because the near-wall regions drain first and thus the evaporation rate is lower from these locations. Figure 4c, at $t = 3.25$ hr, shows that the coarser side temperatures are higher than the finer side ones. Figure 4d ($t = 5.23$ hr) corresponds to the first transition when the coarser beads region, nearly devoid of water, shows higher temperature (~51 °C) compared to the finer glass beads side, which is completely wet and ~38 °C; this image is nearly at the same time as the dye visualization images seen in Figures 2i, 2j, and 2l. This large difference in the surface temperature of the finer and the coarser glass beads is related to the higher evaporation rate from the finer beads side. At $t = 6.73$ hr, (Figure 4e) evaporation is almost entirely from finer beads side. Figure 4f, captured during the second transition, shows the increase of surface temperature of the finer beads, as the water content and the evaporation rate reduce. Finally, Figure 4g, captured during the second stage when evaporation rate is very low, shows high temperatures on both coarser and finer beads' sides.

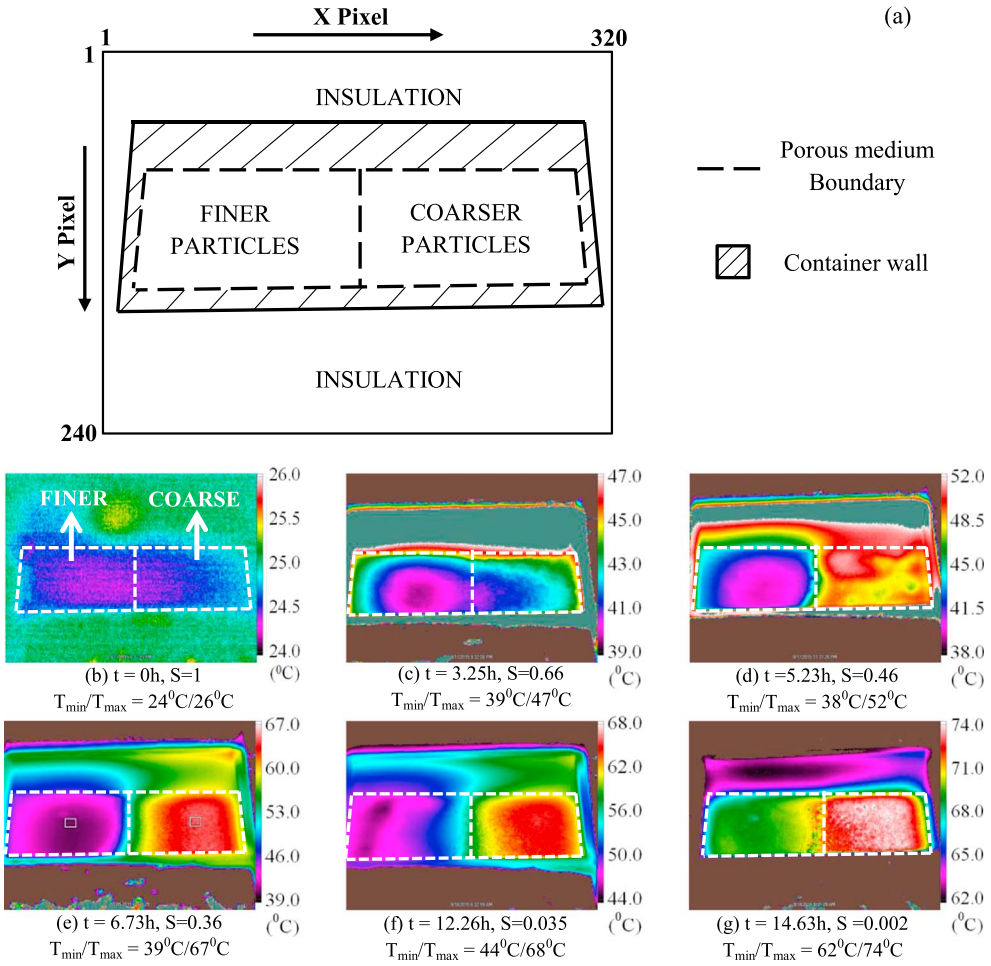

Figure 4. Snapshots of the thermal images of the top surface of the porous medium for side-by-side configuration at different times. A schematic (a) shows different regions seen in an IR image. Purple and red color represents colder and hotter regions respectively. Left and right halves of the thermal images correspond to the top surfaces of the finer (0.10- to 0.16-mm diameter) and the coarser (0.70- to 0.85-mm diameter) glass beads, respectively. Heat flux received by the top surface = 1,200 W/m^2. Note that infrared images were captured at an interval of ~30 min. The exposed boundary of the porous medium in the infrared images is outlined by a dashed white line. Also shown is the interface separating the two glass bead sizes.

We use the IR images to generate evaporation maps. Note that each pixel in an IR image represents the local temperature, which we have converted into the local evaporation rate using equation (5). Figure 5 shows the contours of the evaporation rate corresponding to the IR images (Figures 4c and 4e), respectively. The differing evaporation rates in the finer and coarser regions are clearly seen in both the cases. The evaporation rates on the finer (wetter) side agree with calculated values shown in Figure 3, whereas the evaporation rates in the coarser region show higher values. When the surface is dry, the calculation of evaporation rate from equation (5) becomes very sensitive to the values of convective losses calculated using the *Nu-Ra* correlation (Eq. (3)) which has inherent uncertainty of ~10%. The SEB model offers a way to obtain evaporation maps based on measured surface temperature distributions, and certainly allows us to distinguish between high and low evaporating regions.

We now look at the variation of surface temperature with time in two regions, one in the coarser beads and the other in the finer beads. Average temperatures were obtained over two square boxes (10 pixels by 10 pixels), marked in Figure 4e. The locations of these square regions were fixed for all the thermal images. Figure 6a shows the variations of the average temperature in these two boxes with time. Black diamond and filled circle markers represent the coarser (0.70- to 0.85-mm diameter) and the finer (0.10- to 0.16-mm diameter) glass beads, respectively. Till the first transition, the two surface temperatures are nearly

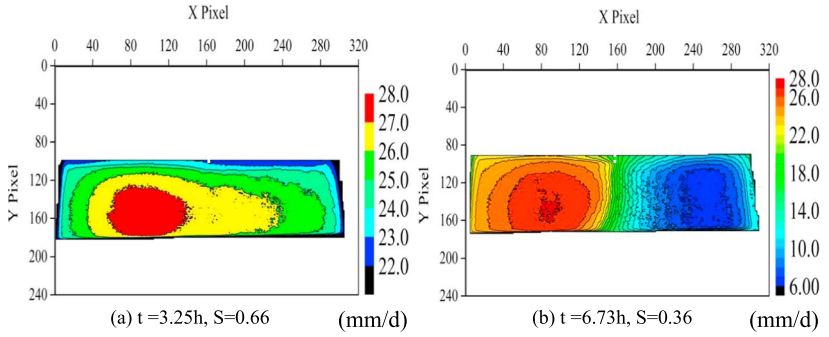

Figure 5. Contours of the evaporation rate generated from two infrared images, viz., Figures 4c and 4e. The maps are generated when the heat flux received by the top surface is ~1,200 W/m^2.

constant with time, but with the coarser side warmer than the finer side by about 5 °C. After the first transition, a sudden increase in the surface temperature of the coarser glass beads is seen and the temperature difference between the coarser and finer sides is as high as 25 °C. A slow increase in the surface temperature of the finer glass beads is seen between the first and the second transitions. After the second transition, there is a steep increase in the finer beads surface temperature and then both the surface temperatures are nearly same, close to 72 °C.

The surface temperature is an indirect indicator of evaporation rate. A decrease in evaporation rate, and thus a reduced contribution of latent heat loss, is compensated by an increase in surface temperature, increasing the convective and radiative heat losses to the ambient. For the incident heat flux of 1,200 W/m^2, the evaporation rate (E_w) is estimated using equation (5); its variation with time is shown in Figure 6b along with the experimentally obtained values. We can estimate E_w using equation (5) in two different ways: (a) based on the average T_s calculated individually from the IR images on the coarser and finer sides and (b) based on the local T_s. From the measured average surface temperature values (T_s) on each side (coarse and fine), we calculate, using equation (5), the individual evaporation rates, which are summed up to give the total evaporation rate. In the second method, we obtain the evaporation maps, as shown in Figure 5, using the temperature maps. Then the average evaporation rate is obtained by taking the areal average of the evaporation distribution. The average evaporation rates predicted by the SEB are higher than the experimental values, with the method (second method) using the evaporation maps doing slightly better by about ~5%. In spite of the several assumptions, the SEB (both the approaches) quite accurately captures the variation of the evaporation rate. The slight overprediction of the evaporation rate, following equation (5), in stage 1 could be majorly due to uncertainties in measurement of T_s and I_{total} and in estimating the convective heat loss.

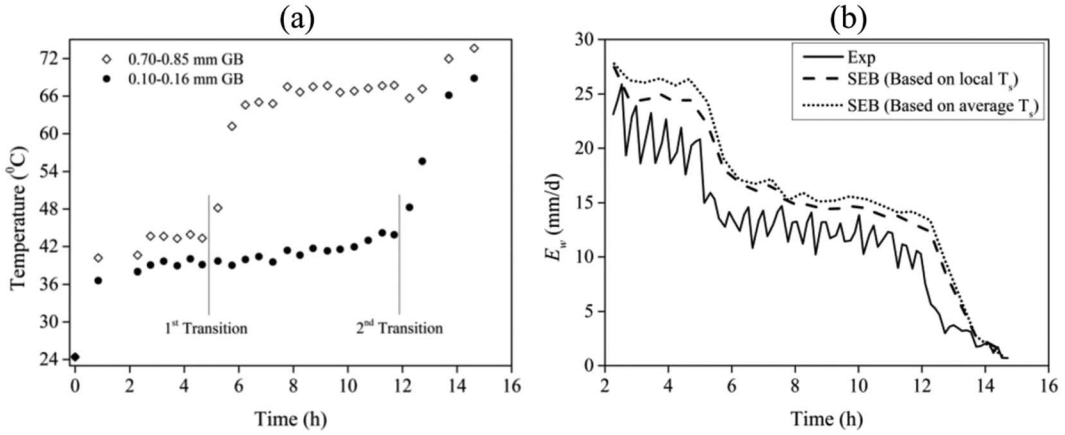

Figure 6. Variation of the average temperatures within the small square box (see Figure 4e) with time (a). Filled circle and open diamond marker represent the average surface temperature for the coarser and the finer regions, respectively. The predicted and experimentally obtained values of E_w is seen plotted versus time in (b).

Table 1
Various Parameters and their Values used in Creating the Porous Medium

Lower beads size (mm); height (mm)	Upper beads size (mm); height (mm)	L_{cap} finer (mm)	L_{cap} coarser (mm)	Water mass for saturation (g)	Total porosity (%)
0.70–0.85; 73	**0.10–0.16; 10**	122	34	**86.40**	**33.20**
0.70–0.85; 73	**0.20–0.30; 10**	94	34	**90.42**	**34.88**
0.70–0.85; 73	0.40–0.50; 10	70	34	91.82	35.28
0.70–0.85; 73	0.50–0.60; 11	46	34	93.46	35.39
1.0–1.2; 73	0.70–0.85; 10	34	31	93.45	35.66
1.4–1.6; 73	0.70–0.85; 10	34	26	92.17	35.45
2.0–2.2; 73	0.70–0.85; 10	34	21	91.14	35.17
2.5–3.0; 73	**0.70–0.85; 10**	34	18	**87.88**	**34.31**

Note. Values mentioned in bold font represent the experiments in which the finer glass beads managed to enter into the voids of the coarser glass beads (either between the coarser glass beads and the boundaries or in between the coarser glass beads), which also reflect in the corresponding values of water mass for saturation (column 5) and porosity (column 6).

The error in convective heat loss calculation stems from the *Nu-Ra* correlation used to calculate h, not being applicable to the current configuration, and because of the inherent uncertainty in the correlation itself. Note that uncertainty in T_s measurement is small and the error, in estimating the rate of evaporation, due to this will be smaller. Similarly, the estimated radiation heat loss carries with it a small inaccuracy which can be ignored. Note that in the first hour, we estimated the heat stored (in the porous medium) to be about ~ 35% of the total incident energy. Between 1 and 2 hr the increment in the heat stored is ~3%. From 2 to 5 hr, the additional heat stored is ~2% of the incident heat energy. During the first transition, 5 to 6 hr, the heat storage is ~12% (most of this heat is stored in the coarser region), and again after this transition, ~6–12 hr, the storage term will be negligible.

4.2. Thin Layer of Finer Beads Over Coarser Beads: Altering the Capillary Film Length

In this section we study the evaporation characteristics of horizontal textural layering, with the FoC configuration. First, we present evaporation characteristics and thermal images for one case and show that layering dramatically changes the CRP regime and delays the transition (increases the L_{cap}) compared to the homogeneous case. Then we present results on the how bead size ratio changes the capillary film length. In the subsequent section, we discuss results from fluorescein dye visualization for this configuration in shallow container for one bead size ratio.

Here we report experimental findings for a range of fine to coarse diameter ratios; Table 1 lists the experimental parameters and also the L_{cap} values corresponding to the two individual bead sizes. In all the cases the height of the porous medium was such that it was greater than L_{cap}, that is, the evaporation will happen in the capillary-gravity regime and a true transition to second stage is expected. The L_{cap} values are calculated as the product of the height of the container and the saturation value at the end of stage 1. It essentially denotes the drop in the level of water at the end of stage 1 if the drying front would have moved horizontally.

One of the limitations in creating FoC configuration is the diameter ratio of the two sizes. If the ratio is sufficiently small, the finer particles enter into the voids of the coarser particles. Experiments with such a situation are shown in bold font in Table 1. Note that the thickness ($h(F)$) of the upper glass beads is nearly 10 mm in all the experiments which is much lower than its L_{cap} value. The thickness ($h(C)$) of the lower glass beads was 73 mm in all the experiments. In comparison, for a two layered FoC configuration, $h(F)/h(C)$ in Shokri et al. (2010) was 7/19 cm and 22/4 cm, while in Assouline et al. (2014) three cases with 2/48 cm, 6/44 cm, and 12/38 cm were studied; in both these studies, the beads in each of the layers were polydisperse and the bead size ranges in the two layers for the different experiments were fixed.

Evaporation characteristics from one experiment (1.5B0.7T) are shown in Figure 7a. For comparison, evaporation curves for the homogeneous porous media (with glass beads of 0.70- to 0.85- and 1.4- to 1.6-mm diameter) are also shown. The abbreviation, 1.5B0.7T, means 0.70- to 0.85-mm diameter glass beads are on top of 1.4- to 1.6-mm diameter glass beads; this convention is followed for all the cases. Excess water of 9 and 12 g above saturation was used as the initial condition for the porous media in case of *0.70–0.85 mm* and *1.5B0.7T*, respectively. For the experiment with 1.4- to 1.6-mm diameter GB, there was no excess water but the porous medium was fully saturated initially. The slight drops in the evaporation rate for two cases at t ~ 5 hr are when the excess water on top evaporates. After this the evaporation rates are nearly same for all three cases because the IR heat flux is same. For the two homogeneous cases, in the first stage, there is a gradual reduction in the evaporation rates after t = 4.23 hr. In contrast, for the layered case there is hardly any reduction in the value of the evaporation rate till the transition. The nearly constant evaporation rate (from t = 5.43 to 24.27 hr) in its first stage is followed by a rapid decrease. This difference between homogeneous and layered cases is reflected in the mass loss curves. The constant evaporation rate in the case of *1.5B0.7T* suggest the presence of constant surface water till the transition. Almost no reduction in the surface water content, as the total water mass reduces, is achieved by suction applied by the finer glass beads on the

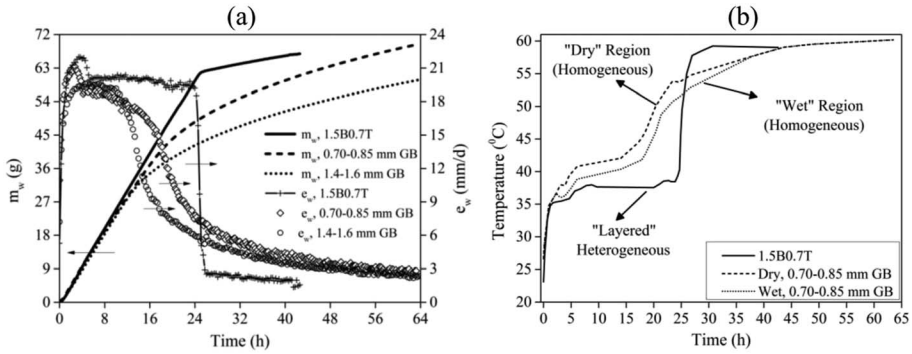

Figure 7. Variation of (a) evaporated mass and evaporation rate versus time from different types of porous media in identical containers. Lines in (a) represent mass loss while markers represent the corresponding evaporation rates plotted on the secondary vertical axis. The corresponding surface temperature variations are shown in (b). Heat flux received by the top surface in all cases was 1,000 W/m^2.

water in the coarser glass beads. After the transition the evaporation rate attains a value that is lower than the value of the evaporation rate in *0.70–0.85 mm GB* at the same instant, implying that after the transition in the layered case the water front has receded much deeper compared to that in the homogeneous case. We note that the duration of CRP increased not only with respect to time but also at transition the saturation was lower or the average water depth (L_{cap}) was higher. In the homogeneous case, during stage 1, evaporation rate decreases not only due to the reduced surface water content, as is evident from the thermal images, but also due to continuously reducing contribution from the receding liquid-vapor interface(s) within the porous medium (Shahraeeni et al., 2012).

Figure 7b shows the variation of the surface temperature of the two porous media with time. For the homogeneous case two regions are visible in the images that we refer to as *wet* and *dry* regions, corresponding to regions of lower and higher temperature. For the layered (FoC) case temperature is averaged throughout the surface. Two points may be noted for the layered case: (1) nearly constant temperature in stage 1 and (2) sudden increase in the surface temperature during the transition. In contrast for case of the homogeneous porous medium during stage 1, the average surface temperature increased nearly 3 °C in 11 hr, and the transition in this case is gradual (Figure 7b). After transition, in both the layered and homogenous cases, surface temperatures are seen higher (~60 °C) corresponding to the low evaporation rates. We see that in case of FoC, the average surface temperature attained nearly 60 °C from 39 °C within 2 hr during transition, which was rapid, compared to more than 10 hr in the homogeneous case, where the transition was more gradual. There is good correspondence between the variations of evaporation rate and surface temperature.

IR images reveal the surface temperature distributions. Figures 8a–8f and 8g–8i show a sequence of thermal images of the top surface for layered (1.5B0.7T) and the homogeneous (0.70- to 0.85-mm diameter GB) porous media respectively. Figure 8a was taken just before the experiment commenced and the surface temperatures are seen to be slightly below the ambient. As the excess water evaporates, the surface temperature increases (Figure 8b), and at this instant (t = 4.67 hr), sharp structures in the thermal image are seen due to the uneven water surface around the beads. During the constant evaporation rate period (~5 to 24 hr, Figures 8b–8d) when the average temperature increases by about 1 °C, most the of the surface (except near the boundary) is at a uniform temperature. In contrast, for the homogeneous case, during stage 1 (~3 to 19 h, Figures 8g–8i), distinct regions of *higher* and *lower* temperatures, representing dry and wet surfaces respectively, are seen clearly (Figure 8h). The reduction in evaporation due to reduction in the surface water is accompanied by formation and growth of the warmer regions; the presence of a warm, *dry* island is clearly visible in Figure 8h. No such islands are seen for the layered case consistent with the observation that the evaporation rate is constant in stage 1, and the surface is always wet. Compared to the homogeneous case, surface water in the FoC case vanishes quite rapidly (within 1 hr), from Figure 8d at t = 23.89 hr to Figure 8f, taken just before the transition, at t = 24.90 hr; simultaneously, the surface temperature, which is more uniform than the homogenous case, increases rapidly with time. Only at this stage, nonuniformity sets in and we can clearly distinguish the *wet* zones and the *dry* regions.

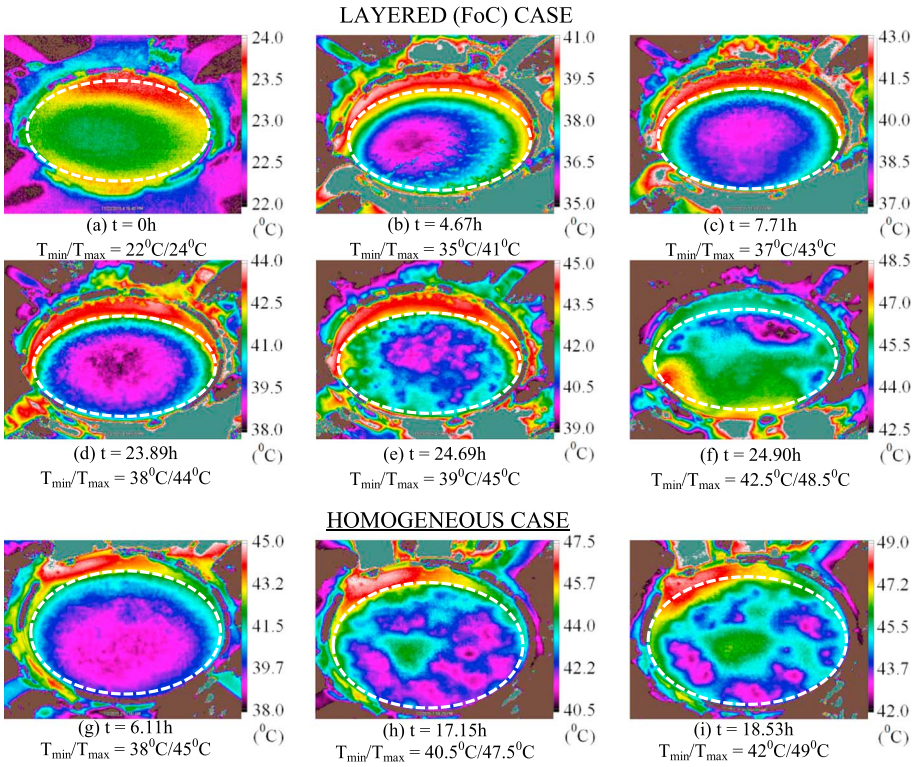

Figure 8. Snapshots (a–f) of the thermal images of the top surface at different times for layered porous medium in finer over coarser (FoC) configuration 1.5B0.7T. Purple and red color represents the colder and the hotter regions respectively. (g–i) The thermal images for a homogeneous porous medium consisting of 0.70- to 0.85-mm diameter glass beads only. Heat flux received by the top surface for both the cases was nearly 1,000 W/m^2. The exposed boundary of the porous medium is outlined by a dashed white line.

For a fixed IR image, since the temperature fluctuation across different pixels is negligible in the FoC case, we chose T_s to represent the surface temperature averaged throughout the exposed top surface; its variation is seen in Figure 7b. The SEB (equation (5)) may be used to estimate the evaporation rate from the surface temperature for the (FoC) configuration, as was done for the side-by-side case. Figure 9 shows the calculated evaporation; the incident total heat flux was 1,000 W/m^2, and the value of k_{loss} was higher than the side-by-side case; it was 4.45 W/m^2 K and 1.06 W/m^2 K for the FoC and side-by-side cases, respectively. The calculated evaporation rate, either through the average surface temperature or through averaging of local evaporation rates based on the evaporation maps, from the model agrees reasonably well (within ±2%) with measured evaporation rate, again indicating the close quantitative relation between surface temperature and evaporation rate. SEB (equation (5)) is able to predict the rate of evaporation knowing the surface temperature for both the types of layering.

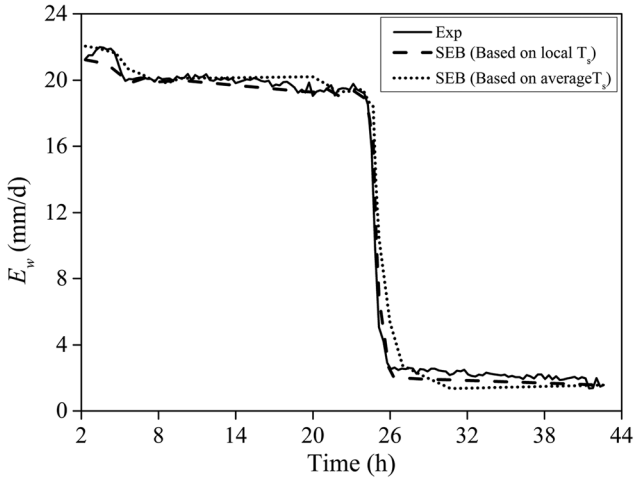

Figure 9. Estimated evaporation rates, using the two approaches, at different instants from equation (5) for the finer over coarser configuration. Also shown is the variation of the experimentally obtained evaporation rate.

4.2.1. Effect of Beads Sizes on Capillary Film Length for FoC

In the previous section we saw that layering with FoC configuration dramatically alters the evaporation characteristics, in particular it delays transition. In this section we present quantitative information on how the capillary film length is altered as the ratio of finer-to-coarser bead diameter is varied. Two sets of experiments were conducted, *Set 1*, where we fixed the coarser glass beads (0.70–0.85 mm) at the bottom of the porous medium and varied the finer glass beads sizes on the top from 0.10–0.16 to 0.5–0.6 mm in diameter, and *Set 2* where we fixed the finer glass beads (0.70–0.85 mm) at the top and the coarser glass beads sizes at the bottom were varied from 1.0–1.2 to 2.5–3.0 mm in diameter. All

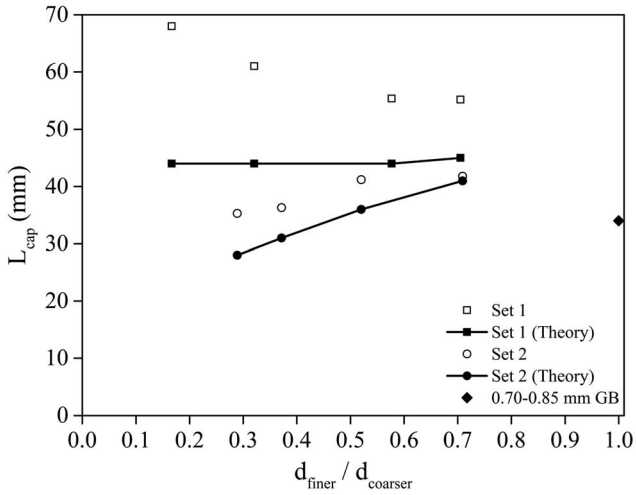

Figure 10. Variation in L_{cap} for different cases versus diameter ratio of the finer top and coarser bottom particles. Also seen are L_{cap} values (solid black lines with markers) calculated using the theory given in Shokri et al. (2010) and Assouline et al. (2014).

the experiments were carried out in the same container (glass beaker) and had similar depths and same amount of excess water initially; Table 1 lists the parameters for the two sets.

In all the experiments listed in Table 1, two points were common with 1.5B0.7T case discussed above: (1) the evaporation rate in the first stage was close to the bare water case and (2) the transition to second stage was steep. Figure 10 shows the L_{cap} values plotted versus the diameter ratio ($d_{finer}/d_{coarser}$). For reference, L_{cap} for a homogeneous porous medium consisting only of 0.70- to 0.85-mm diameter GB is 34 mm and is marked in Figure 10. Figure 10 also shows the corresponding L_{cap} values according to the theory proposed by Shokri et al. (2010) and Assouline et al. (2014) for the FoC configuration:

$$L_{cap}(\text{FoC}) = L_{cap}(C) + h(F) \tag{6}$$

where C and F represent coarser and finer, respectively, and $h(F)$ is the finer beads layer height. Equation (6) was experimentally shown to hold if $h(C) > L_{cap}(C)$ and $h(F) \ll L_{cap}(F)$. In the present set of experiments both of these conditions are satisfied. Equaton (6) implies that the effective L_{cap} is essentially L_{cap} of the coarser beads to which is added the finer beads layer height, and its value is independent of the finer bead size. Thus, for Set 1, since $h(F) \sim 10$ mm and $L_{cap}(C) = 34$ mm, the L_{cap} (FoC) according to equation (6) is constant = 44 mm, shown as filled squares in Figure 10. The values of L_{cap} (FoC) from the experiments (open squares in Figure 10) from this set are higher and are also not constant but increase as the finer bead size reduces. Probably the decreasing finer glass beads size strengthened the capillary film(s) thereby increasing the L_{cap}value. For the Set 2 cases, the agreement between theoretically predicted L_{cap} values (filled circles in Figure 10) with those from experiments (open circles) is better, with experimentally found L_{cap} values being slightly higher. The results from these experiments suggest that diameter ratio is not the only governing parameter in determining L_{cap} for the FoC configuration. The dynamics at the interface of the two sizes is perhaps important and needs further investigation, and the contribution of individual particle sizes to L_{cap} cannot be ignored. The experimental results of Shokri et al. (2010) followed equation (6) for the FoC configuration; there was a small difference between the experimental results of Assouline et al. (2014) and the predictions of equation (6). As mentioned above, the main difference between our experiments and theirs is that the beads in our case were nearly monodisperse, whereas in their case the beads had a range of sizes. And in their experiments the relative layer heights were changed, whereas in our experiments the fine-to-coarse bead diameter was changed. Note that for a fixed homogeneous porous medium, L_{cap} is not constant (Lehmann et al., 2008; Sadeghi et al., 2014a, 2014b); it depends on various variables such as the evaporation rate itself.

4.3. Visualization Using Fluorescein Dye for Thin Layer of Finer Beads Over Coarser Beads in a Shallow Container

The fluorescein dye visualization gives further insight into the evaporation processes in layered porous medium with FoC configuration. For the visualization we used a shallow container for which the transition is due to depletion of water. However, the essential processes near the surface and the interface will be same as for the cases where height of the porous medium is greater than L_{cap}. In this experiment we use a 5-mm thick layer of finer (0.40- to 0.50-mm diameter, 0.45-mm mean diameter) glass beads on top of 32-mm thick layer of coarser (0.70- to 0.85-mm diameter) glass beads. The height of the acrylic box was 40 mm, and the total height of the porous medium was 37 mm. The prepared sample, having a small amount of fluorescein dye, was saturated with an overall porosity of approximately 35.90%. A series of snapshots of top and side views of the porous medium were taken during evaporation at different instants and are shown in Figure 11. For comparison, also shown are the dye images during evaporation of a homogeneous (0.45-mm mean diameter GB) porous medium. The height of the homogeneous porous medium was 25.4 mm, and its porosity was 36.5%. The heights of both the porous media were smaller than their respective L_{cap} values and almost all water evaporates in the capillary regime. Heat flux received by the top surface of

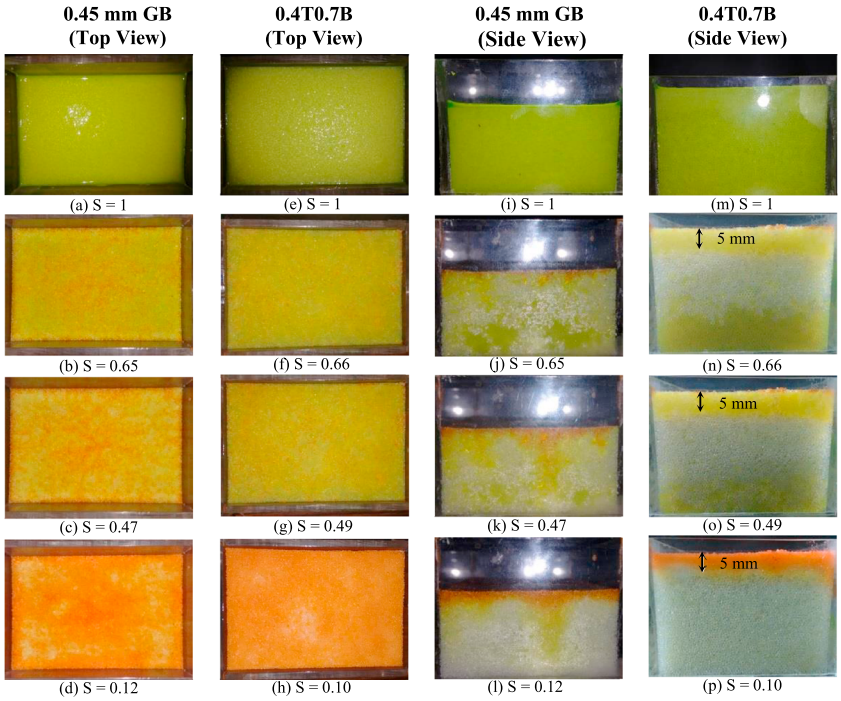

Figure 11. A series of snapshots of the two porous medium, one with 0.40- to 0.50-mm glass beads (GB) alone and the other with finer over coarser (FoC) configuration, at different degree of saturation. Columns 1 and 3 show the top and side views of the homogeneous porous medium, respectively. Columns 2 and 4 show the top and side views respectively of the FoC configuration. For FoC case, 5-mm thick 0.40- to 0.50-mm GB were placed over 32 and 0.70- to 0.85-mm GB. Heat fluxes received by the top surfaces in case of the homogeneous and FoC porous media were about 1,200 W/m^{2}and 1,000 W/m^2, respectively. *S* represents the saturation values.

homogeneous and 0.4T0.7B (0.40- to 0.50-mm diameter beads on top and 0.70- to 0.85-mm diameter particles at the bottom) porous media were about 1,200 W/m^2 and 1,000 W/m^2, respectively. This difference in heat flux was not found to change the evaporative characteristics much (Kumar, 2016).

Nearly 90% of water was observed to evaporate in the first stage for both the cases and the transition was forced due to depletion of water in the container. Figures 11a–11d and 11i–11lshow the fluorescein dye deposition patterns in the top and side views of the homogeneous porous medium, respectively. The respective top and side views of 0.4T0.7B case are seen in Figures 11e–11h and Figure 11m–11p. In the initially saturated state (Figures 11a, 11e, 11i, and 11m) or $S = 1$, uniformly distributed green color is seen throughout the porous media. At $S = 0.66$, that is, when about 34% of the water has been lost due to evaporation, for the homogeneous (0.45-mm diameter beads) case the boundary regions near the side walls are drained of water starting from the top (Figure 11j); at the same *S* value, for the layered case of 0.4T0.7B, the draining starts from below the interface of the two layers (Figure 11n). Some dye deposits are seen in the homogeneous case (Figures 11b and 11j), while hardly any deposits are hardly observed in 0.4T0.7B case (Figures 11f and 11n). The few deposits in the layered case appear when excess water evaporates and leaves the dye particles on the beads at the top.

A remarkable observation is that the nearly dry particles (white color) are sand witched between two saturated zones for the layered case, as seen in Figure 11n. Smaller void sizes in the finer glass beads suck water from the coarser glass beads, via the interfacial glass beads, as long as the hydraulic connections are maintained. First stage is sustained as long as the finer glass beads were able to pull water from the coarser ones. At a lower saturation value, for example, S~0.50, fluorescein deposits are clearly seen in the homogeneous case (Figures 11c and 11k), while there is no notable change, in terms of deposition, in the layered case (Figures 11g and 11o) when compared to its condition at $S = 0.67$. The two completely saturated zones are still present but have gone apart now as seen in Figure 11o with the thickness of green color in the top being equal to the depth of the finer glass beads (5 mm). Just after transition, S~0.10, uniformly

distributed orange fluorescein dye deposits is seen in both the layered and homogeneous cases (Figures 11d and 11h). In the side views (Figures 11l and 11p) we see that the particles are deposited within a thin layer (nearly 10 particle layers) for the homogeneous case while its thickness seems to be equal to the finer glass beads height in 0.4T0.7B case (Figure 11p). The dramatic differences between the homogeneous and FoC case in both the evaporation characteristics and surface thermal images are understood better from these visualization pictures.

5. Discussion and Conclusions

In order to understand the effect of textural layering on evaporation we conducted experiments with nearly monodisperse glass beads for two basic configurations: (1) side by side packed differently sized glass beads and (2) FoC. In all the cases constant IR radiation of about 1,000 W/m^2 was used and the evaporation rate was measured and the evaporation process was studied using the fluorescein dye technique and thermal imaging. For FoC cases we present two different configurations: (a) fixed finer glass beads on top and varying coarser glass beads' sizes at the bottom and (b) fixed coarser glass beads at the bottom and varying finer beads' sizes at the top.

In side-by-side orientation, the finer glass beads suck out water from the coarser glass beads which act as the source. As a result the coarser glass beads dry out and their contribution toward the total evaporation rate reduces quickly; evidence for this is clear from the thermal images. As the coarser beads lose water, water remains to be present on the surface of the finer glass beads. Because of the unequal contribution toward the total evaporation rate, the surface temperature of the coarser glass beads is higher and the average surface temperature difference between the coarser and the finer glass beads was as high as 25–26 °C for a heat load of 1,000 W/m^2. For this configuration, two distinct transitions in the evaporation rate, the first corresponding to drying of the coarser beads and the second to transition to second stage in the finer beads, were observed. This study can be extended to multiple sizes stacked side by side in order to control the water transport effectively and hence the moisture loss from soils.

For the CoF configuration (the experimental observations are discussed in detail in the supporting information) the coarser glass beads were found unable to pull water from the finer glass beads leading to an early transition. Considerably reduced (effective) hydraulic conductivity value in CoF compared to its value for the finer case alone has been recently reported (Sadeghi et al., 2014a, 2014b) to be responsible for the early transition. Here the duration of the first stage is approximately equivalent to the amount of water in the coarser glass beads on the top; essentially the finer beads do not play any role. Since the coarser layer is unable to pull water from the finer layer, even a small size difference leads to a shortened CRP stage and thus an early transition.

In FoC configuration the depth of the glass beads on the top was much smaller compared to the depth of the coarser glass beads at the bottom. In both the cases, viz., *fixed finer size with coarser size varied (Set 2)* or *fixed coarser size with finer size varied (Set 1)* the duration of the first stage of evaporation, that is, the duration of CRP, increased significantly when compared to CRP duration for the bottom beads only. The finer particles at the top pull water from the coarser glass beads at the bottom. This pull is distributed uniformly on the interface between the two sizes which leads to continuous and uniform wetting of the top surface. Contraction of water films at the top, seen in the homogeneous porous medium consisting of monodisperse spheres during CRP, was not observed in this case. Since the top surface of the porous medium is (nearly) completely wet till the transition, the usual gradual decrease in the evaporation rate in CRP regime was not observed; a true CRP is achieved in this configuration. CRP was followed by a rapid transition and a steep drop in the evaporation rate. The theoretical estimates by Shokri et al. (2010) and Assouline et al. (2014) agreed well for the experiments of Set 2. However, for the experiments of Set 1 the disagreement is large.

Experimentally obtained L_{cap} values in the present case with nearly monodisperse glass beads (homogeneous case) did not follow the theoretical prediction by Lehmann et al. (2008) who obtained L_{cap} essentially for a range of particle sizes (having a wide pore size distribution). Particle sizes and range both are crucial in determining L_{cap} of a homogeneous and a layered porous medium. For the FoC case, additional complexity arises when the chosen particle sizes are such that the finer particles can enter into the voids of the coarser particles. This intermixing of the particles in a layered porous medium is expected to affect the overall L_{cap}

significantly; this effect cannot be ignored in Shokri et al. (2010) and Assouline et al. (2014). Thus prediction of L_{cap} for the FoC configuration needs further and detailed study with different combinations of particle sizes.

In both the types of layering, and in the homogeneous case, a surface energy budget gave, using the measured surface temperature, estimates of evaporation rate, which agreed reasonably well with the measured evaporation rates; for side-by-side layering the accuracy of the model was lower (~12%). Note that the model cannot be directly used in the transient cases when porous medium temperature changes rapidly with time and heat storage term is nonnegligible. However, if the ground heat flux (sensible term) is known then it can be included in equation (5). In field conditions, knowing the surface temperature and the ambient conditions, SEB may be used to estimate evaporation rates from soils and get an idea of the surface moisture at small spatial scales with surface temperature captured from IR cameras. The field conditions are of course more complex and uncertainties are larger. The controlled IR heating along with simultaneous evaporation and surface temperature measurements and fluorescein dye visualization have given a good physical picture of the processes. In addition, the quantitative information from these controlled experiments may be used to validate existing numerical models or develop new ones for drying of porous media with horizontal and vertical layering, which finally can be applied to field situations.

Acknowledgments
Financial support from Robert Bosch Center for Cyber Physical Systems (project RBCCPS/ME/JHA/PC-0013) is gratefully acknowledged. Funds for purchase of the precision balance, obtained from Divecha Centre, IISc, are gratefully acknowledged. The data in this study are available here doi:10.6084/m9.figshare.5745594.

References

Aminzadeh, M., & Or, D. (2013). Temperature dynamics during nonisothermal evaporation from drying porous surfaces. *Water Resources Research*, *49*, 7339–7349. https://doi.org/10.1002/2013WR014384

Aminzadeh, M., & Or, D. (2014). Energy partitioning dynamics of drying terrestrial surfaces. *Journal of Hydrology*, *519*, 1257–1270.

Assouline, S., Kfir, N., Rivka, G., Philippe, L., & Prat, M. (2014). Analysis of the impact of surface layer properties on evaporation from porous systems using column experiments and modified definition of characteristic length. *Water Resources Research*, *50*, 3933–3955. https://doi.org/10.1002/2013WR014489

Bange, G. G. J. (1953). On the quantitative explanation of stomatal transpiration. *Acta Botanica Neerlandica*, *2*(3), 255–297. https://doi.org/10.1111/j.1438-8677.1953.tb00275.x

Brown, H. T., & Escombe, F. (1900). Static diffusion of gases and liquids in relation to the assimilation of carbon and translocation in plants. *Proceedings of the Royal Society of London*, *67*(435–441), 124–128.

Bruch, P. G. (1993). Laboratory study of evaporative fluxes in homogeneous and layered soils (PhD thesis).

Chauvet, F., Duru, P., & Prat, M. (2010). Depinning of evaporating liquid films in square capillary tubes: Influence of corners' roundedness. *Physics of Fluids*, *22*(11), 112113-1–12113-14.

Chauvet, F., Duru, P., Sandrine, G., & Prat, M. (2009). Three periods of drying of a single square capillary tube. *Physical Review Letters*, *103*(12), 124502. https://doi.org/10.1103/PhysRevLett.103.124502

Cooke, J. R. (1967). Some theoretical considerations in stomatal diffusion: A field theory approach. *Acta Biotheoretica*, *17*(3), 95–124.

Daamen, C. C., & Simmonds, L. P. (1996). Measurement of evaporation from bare soil and its estimation using surface resistance. *Water Resources Research*, *32*(5), 1393–1402. https://doi.org/10.1029/96WR00268

Eagleman, J. R., & Jamison, V. C. (1962). Soil layering and compaction effects on unsaturated moisture movement. *Soil Science Society of America Journal*, *26*(6), 519–522.

Gardner, H. R., & Hanks R. J. (1966). Effect of sample size and environmental conditions on evaporation of water from soil. USDA Conserv. Res. Rep. 9. (pp. 14).

Huang, M., Barbour, S. L., Elshorbagy, A., Zettl, J., & Si, B. C. (2013). Effects of variably layered coarse textured soils on plant available water and forest productivity. *Procedia Environmental Sciences*, *19*, 148–157.

Huang, M., Philip, G. B., & Barbour, S. L. (2013). Evaporation and water redistribution in layered unsaturated soil profiles. *Vadose Zone Journal*, *12*(1), 1–14.

Kalma, J. D., McVicar, T. R., & McCabe, M. F. (2008). Estimating land surface evaporation: A review of methods using remotely sensed surface temperature data. *Surveys in Geophysics*, *29*, 421–469.

Keita, E., Faure, P., Rodts, S., & Coussot, P. (2013). MRI evidence for a receding-front effect in drying porous media. *Physical Review E*, *87*(6), 062303. https://doi.org/10.1103/PhysRevE.87.062303

Keita, E., Koehler, S. A., Faure, P., Weitz, D. A., & Coussot, P. (2016). Drying kinetics driven by the shape of the air/water interface in a capillary channel. *European Physical Journal E: Soft Matter*, *39*(2), 23–23.

Ketelaars, A. A. J., Pel, L., Coumans, W. J., & Kerkhof, P. J. A. M. (1995). Drying kinetics: a comparison of diffusion coefficients from moisture concentration profiles and drying curves. *Chemical Engineering Science*, *50*(7), 1187–1191.

Kumar, N. (2016). Evaporation of water from soil-like, leaf-like surfaces and unconventional porous media (PhD thesis), Bangalore: Indian Institute of Science.

Kumar, N., & Arakeri, J. H. (2018a). Evaporation From Confined Porous Media Due to Controlled IR Heating From Above. *Transport in Porous Media*, *125*, 311–340.

Kumar, N., & Arakeri, J. H. (2018b). Sustained high evaporation rates from porous media consisting of packed circular rods. *International Journal of Thermal Sciences*, *133*, 299–306. https://doi.org/10.1016/j.ijthermalsci.2018.07.035

Lehmann, P., & Or, D. (2009). Evaporation and capillary coupling across vertical textural contrasts in porous media. *Physical Review E*, *80*(4), 046318. https://doi.org/10.1103/PhysRevE.80.046318

Lehmann, P., Shmuel, A., & Or, D. (2008). Characteristic lengths affecting evaporative drying of porous media. *Physical Review E*, *77*(5), 056309. https://doi.org/10.1103/PhysRevE.77.056309

Li, X., Scott, X. C., & Salifu, K. F. (2013). Soil texture and layering effects on water and salt dynamics in the presence of a water table: A review. *Environmental Reviews*, *22*(1), 41–50.

Lloyd, J. R., & Moran, W. R. (1974). Natural convection adjacent to horizontal surface of various planforms. *Journal of Heat Transfer*, *96*(4), 443–447.

Mauder, M., Jegede, O. O., Okogbue, E. C., Wimmer, F., & Foken, T. (2007). Surface energy balance measurements at a tropical site in West Africa during the transition from dry to wet season. *Theoretical and Applied Climatology*, *89*(3–4), 171–183.
Modaihsh, A. S., Robert, H., & Kirkham, D. (1985). Soil water evaporation suppression by sand mulches. *Soil Science*, *139*(4), 357–361.
Or, D., Lehmann, P., Shahraeeni, E., & Shokri, N. (2013). Advances in soil evaporation physics—A review. *Vadose Zone Journal*, *12*(4), 1–16.
Pel, L., Ketelaars, A. A. J., Adan, O. C. G., & van Well, A. A. (1993). Determination of moisture diffusivity in porous media using scanning neutron radiography. *International Journal of Heat and Mass Transfer*, *36*(5), 1261–1267.
Pillai, K. M., Prat, M., & Marcoux, M. (2009). A study on slow evaporation of liquids in a dual-porosity porous medium using square network model. *International Journal of Heat and Mass Transfer*, *52*(7), 1643–1656.
Poulovassilis, A., & Psychoyou, M. (1985). Steady-state evaporation from layered soils. *Soil Science*, *140*(6), 399–405.
Qiu, G. Y., Ben-Asher, J., Yano, T., & Momii, K. (1999). Estimation of soil evaporation using the differential temperature method. *Soil Science Society of America Journal*, *63*(6), 1608–1614.
Qiu, G. Y., Peijun, S., & Liming, W. (2006). Theoretical analysis of a remotely measurable soil evaporation transfer coefficient. *Remote Sensing of Environment*, *101*(3), 390–398.
Ross, B. (1990). The diversion capacity of capillary barriers. *Water Resources Research*, *26*(10), 2625–2629. https://doi.org/10.1029/WR026i010p02625
Sadeghi, M., Tuller, M., Gohardoust, M. R., & Jones, S. B. (2014a). Column-scale unsaturated hydraulic conductivity estimates in coarse-textured homogeneous and layered soils derived under steady-state evaporation from a water table. *Journal of Hydrology*, *519*, 1238–1248.
Sadeghi, M., Tuller, M., Gohardoust, M. R., & Jones, S. B. (2014b). Reply to comments on "Column-scale unsaturated hydraulic conductivity estimates in coarse-textured homogeneous and layered soils derived under steady-state evaporation from a water table"[J. Hydrol. 519, 1238–1248]. *Journal of Hydrology*, *529*(2015), 1277–1281.
Schlünder, E. U. (1988). On the mechanism of the constant drying rate period and its relevance to diffusion controlled catalytic gas phase reactions. *Chemical Engineering Science*, *43*(10), 2685–2688.
Shahraeeni, E., Lehmann, P., & Or, D. (2012). Coupling of evaporative fluxes from drying porous surfaces with air boundary layer: Characteristics of evaporation from discrete pores. *Water Resources Research*, *48*, W09525. https://doi.org/10.1029/2012WR011857
Shahraeeni, E., & Or, D. (2011). Quantification of subsurface thermal regimes beneath evaporating porous surfaces. *International Journal of Heat and Mass Transfer*, *54*(19), 4193–4202.
Sherwood, T. K. (1929). The drying of solids—II. *Industrial and Engineering Chemistry*, *21*(10), 976–980.
Shokri, N., Lehmann, P., & Or, D. (2010). Evaporation from layered porous media. *Journal of Geophysical Research*, *115*, B06204. https://doi.org/10.1029/2009JB006743
Shokri, N., Lehmann, P., Vontobel, P., & Or, D. (2008). Drying front and water content dynamics during evaporation from sand delineated by neutron radiography. *Water Resources Research*, *44*, W06418. https://doi.org/10.1029/2007WR006385
Shokri, N., & Or, D. (2013). Drying patterns of porous media containing wettability contrasts. *Journal of Colloid and Interface Science*, *391*, 135–141.
Srinilta, S., Nielsen, D. R., & Kirkham, D. (1969). Steady flow of water through a two-layer soil. *Water Resources Research*, *5*(5), 1053–1063. https://doi.org/10.1029/WR005i005p01053
Stefan, M. J. (1881). Uber die Verdampfnngauseinem kreisf6rmig oderelliptischbegrenztenBecken. - Sitzungsber. Kais.Akad. Wiss., Wien. Mathem. - naturwiss., Cl. II, LXXXIII (p. 943).
Suzuki, M., & Maeda, S. (1968). On the mechanism of drying of granular beds. *Journal of Chemical Engineering of Japan*, *1*(1), 26–31.
Thiery, J., Rodts, S., Weitz, D. A., & Coussot, P. (2017). Drying regimes in homogeneous porous media from macro-to nanoscale. *Physical Review Fluids*, *2*(7), 074201. https://doi.org/10.1103/PhysRevFluids.2.074201
Unger, P. W. (1971). Soil profile gravel layers: I. Effect on water storage, distribution, and evaporation. *Soil Science Society of America Journal*, *35*(4), 631–634.
Valckenborg, R. M. E., Pel, L., Hazrati, K., Kopinga, K., & Marchand, J. (2001). Pore water distribution in mortar during drying as determined by NMR. *Materials and Structures*, *34*(10), 599–604.
Wang, X. (2015). Vapor flow resistance of dry soil layer to soil water evaporation in arid environment: An overview. *Water*, *7*(8), 4552–4574.
Warrick, A. W., & Yeh, T. C. J. (1990). One-dimensional, steady vertical flow in a layered soil profile. *Advances in Water Resources*, *13*(4), 207–210.
Willis, W. O. (1960). Evaporation from layered soils in the presence of a water table. *Soil Science Society of America Journal*, *24*(4), 239–242.
Yiotis, A. G., Boudouvis, A. G., Stubos, A. K., Tsimpanogiannis, I. N., & Yortsos, Y. C. (2004). Effect of liquid films on the drying of porous media. *AICHE Journal*, *50*(11), 2721–2737.
Yiotis, A. G., Salin, D., Tajer, E. S., & Yortsos, Y. C. (2012). Drying in porous media with gravity-stabilized fronts: Experimental results. *Physical Review E*, *86*(2), 026310. https://doi.org/10.1103/PhysRevE.86.026310
Yuan, C., Lei, T., Mao, L., Liu, H., & Wu, Y. (2009). Soil surface evaporation processes under mulches of different sized gravel. *Catena*, *78*(2), 117–121.
Zehner, P., & Schlunder, E. U. (1970). Thermal conductivity of packings at moderate temperatures. *Chemie Ingenieur Technik*, *42*(14), 933.
Zhao, W., Yu, P., Ma, X., Sheng, J., & Zhou, C. (2017). Numerical Simulation of Soil Evaporation with Sand Mulching and Inclusion. *Water*, *9*(4), 294.